ADVANCED
SCIENCE NEWS
www.advancedsciencenews.com

NANO MICRO
small

Energy Storage

Phosphorus Enhanced Intermolecular Interactions of SnO$_2$ and Graphene as an Ultrastable Lithium Battery Anode

Lei Zhang, Kangning Zhao, Ruohan Yu, Mengyu Yan, Wangwang Xu, Yifan Dong, Wenhao Ren, Xu Xu,* Chunjuan Tang, and Liqiang Mai*

SnO$_2$ suffers from fast capacity fading in lithium-ion batteries due to large volume expansion as well as unstable solid electrolyte interphase. Herein, the design and synthesis of phosphorus bridging SnO$_2$ and graphene through covalent bonding are demonstrated to achieve a robust structure. In this unique structure, the phosphorus is able to covalently "bridge" graphene and tin oxide nanocrystal through P−C and Sn−O−P bonding, respectively, and act as a buffer layer to keep the structure stable during charging–discharging. As a result, when applied as a lithium battery anode, SnO$_2$@P@GO shows very stable performance and retains 95% of 2nd capacity onward after 700 cycles. Such unique structural design opens up new avenues for the rational design of other high-capacity materials for lithium battery, and as a proof-of-concept, creates new opportunities in the synthesis of advanced functional materials for high-performance energy storage devices.

1. Introduction

Rechargeable lithium ion batteries (LIBs) based on graphite/LiCoO$_2$, since the initial introduction by the Sony corporation, have been widely applied in portable electronic devices and created a revolution in battery technology as well as a marked swing away from the relatively low-voltage, water-based systems such as nickel–cadmium and nickel–metal hydride batteries and high-temperature systems due to their high energy densities, high energy efficiencies and a long life span.[1–7] However, graphite with a low theoretical capacity of 372 mAh g^{-1} results in a device energy density of about 150 Wh kg^{-1}, which is far from the electric vehicles requirements. Thus, it is highly urgent to explore new anode materials with high theoretical capacities to replace graphite in the next-generation high energy LIBs. So far toward high energy density, two types of reactions based on multiple electron transport are being widely researched, namely, alloying reaction (including Si, Ge, Sb, and Sn) and conversion reaction (mainly metal oxides and sulfides).[8–15]

Among those, SnO$_2$ shows high theoretical capacity originating from a two-step multielectron reaction:[16–24]

$$SnO_2 + 4Li^+ + 4e^- = Sn + 2Li_2O \qquad (1)$$

$$Sn + 4.4Li^+ + 4.4e^- = Li_{4.4}Sn \qquad (2)$$
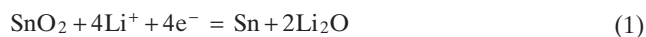
The first step is based on conversion reaction, yielding tin particle and Li$_2$O, followed by the alloying reaction. The two-step reaction results in the large volume expansion–contraction ($\approx$300%).[22,25–29] The huge volume variation and the resulting unstable solid electrolyte interphase (SEI) layer is

L. Zhang, K. N. Zhao, R. H. Yu, Dr. M. Y. Yan, Y. F. Dong,
W. H. Ren, Dr. X. Xu, Dr. C. J. Tang, Prof. L. Q. Mai
State Key Laboratory of Advanced Technology for
Materials Synthesis and Processing
Wuhan University of Technology
Wuhan 430070, China
E-mail: xuxu@whut.edu.cn; mlq518@whut.edu.cn
Dr. L. Q. Mai
Department of Chemistry
University of California
Berkeley, CA 94720, USA
W. W. Xu
Deparment of Mechanical and Industrial Engineering
Louisiana State University
Baton Rouge, LA 70830, USA

generally regarded as the reason of severe capacity fading.[30] Recently, covalent bonds which are chemically stable are able to provide excellent mechanical integrity and good electric connection between two materials.[31–40] Therefore, rational design of unique nanostructure with covalent bonds can improve the cycle performance of tin oxide. In addition, it is also of great significance to correlate the performance with materials structure from the molecular level.

Herein, we demonstrate the design and synthesis of phosphorus covalently crosslinking SnO_2 and graphene (reduced from graphene oxide (GO) the reaction process denoted as SnO_2@P@GO) in which the materials design based on both structure and chemistry is mainly taken into considerations. As a proof of concept, in this unique structure, phosphorus covalently bridges both graphene and tin oxide nanocrystals through P−C and Sn−O−P bonding (**Figure 1**), respectively, and acts as a buffer layer during charging/discharging. In this way, SnO_2@P@GO is able to accommodate the huge volume variation of tin oxide, retain excellent structure integrity and thus, manifest the long-life, high-rate cycling. As a result, when applied as the lithium battery anode, SnO_2@P@GO shows very stable performance, retaining 95% of the 2nd capacity after 700 cycles at a current density of 1 A g^{-1}. Additionally, it should be noted that even after 700 cycles, the tin oxide particles are totally wrapped up by graphene rather than exposed to the electrolyte, which further improves the structure stability.

2. Results and Discussion

The SnO_2@P@GO structure is fabricated through a facile one-step solvothermal method with ethanolamine as solvent

and red phosphorus as P source. Initially, the product is characterized by scanning electron microscopy (SEM) and transmission electron microscopy (TEM) to elucidate the structure feature. The SEM images in Figure S1 (Supporting Information) show typical nanosheet morphology with some ultrasmall particles on it. The low magnification TEM in **Figure 2**A illustrates that the products show crumpled nanosheet morphology. After solvothermal treatment, the sheet morphology of graphene is retained while the surface becomes rather rough, indicating the existence of some particles on it. To further investigate the particles, the dark field TEM image in Figure 2B on the edge shows that graphene nanosheets are uniformly and densely covered by nanoparticles with scarcely void space. The density of nanoparticles is obviously much higher than that without P addition during solvothermal treatment (Figure S2, Supporting Information) and our previous report.[41] Additionally, the fold directly elucidates that the particles coat onto graphene sheets on both sides. Furthermore, magnified TEM image in Figure 2C also shows the homogeneous distribution of nanoparticles with no exposed edges. HRTEM image in Figure 2D reveals the densely packed SnO_2 nanocrystals with (101) plane exposed with lattice fringes of 3.4 Å. The fast Fourier transform image in the inset shows a group of rings consisted of dots which is a typical reflection of polycrystalline. This indicates that the structure is composed of numerous nanoparticles with diameter of 3–5 nm. The SnO_2@P@GO is further unraveled by the typical high angle annular dark field (HAADF) TEM image and the corresponding element mapping images. The elements, carbon, tin, phosphorus, and oxygen, are homogeneously distributed in the sheets. For comparison, SnO_2/GO is produced by the same procedure of SnO_2@P@GO except
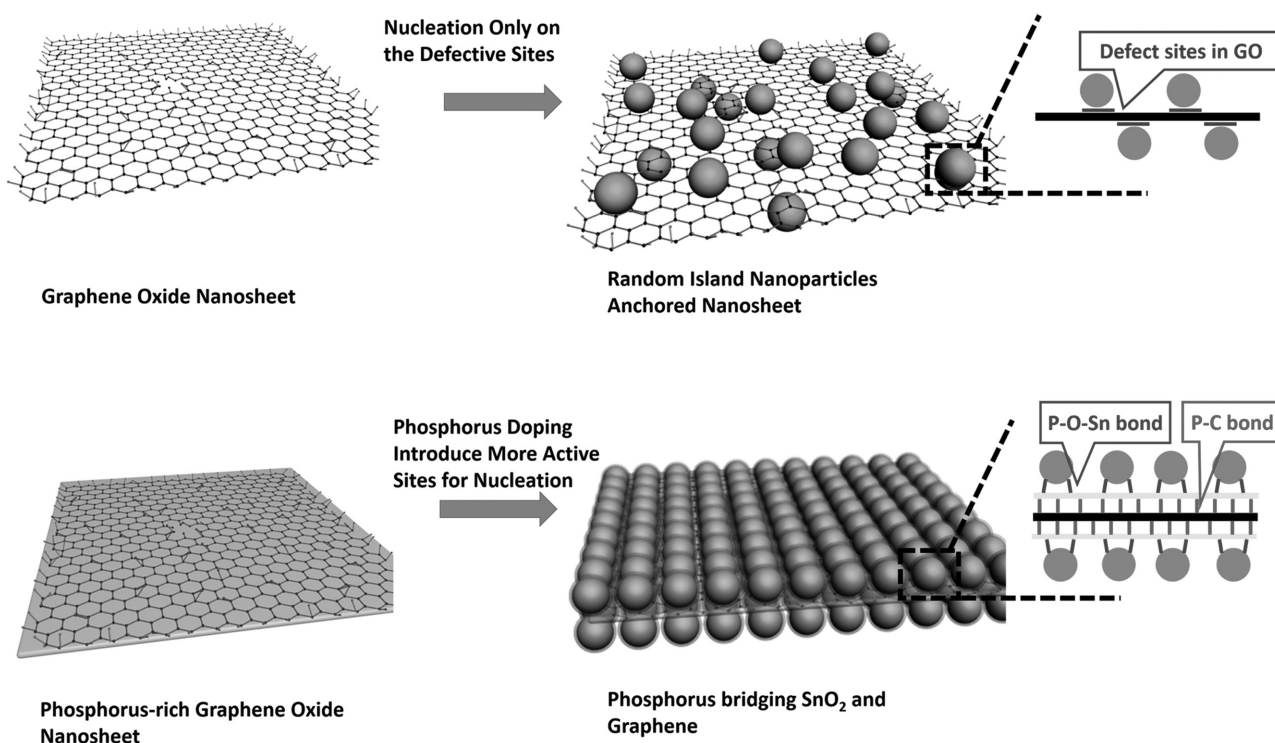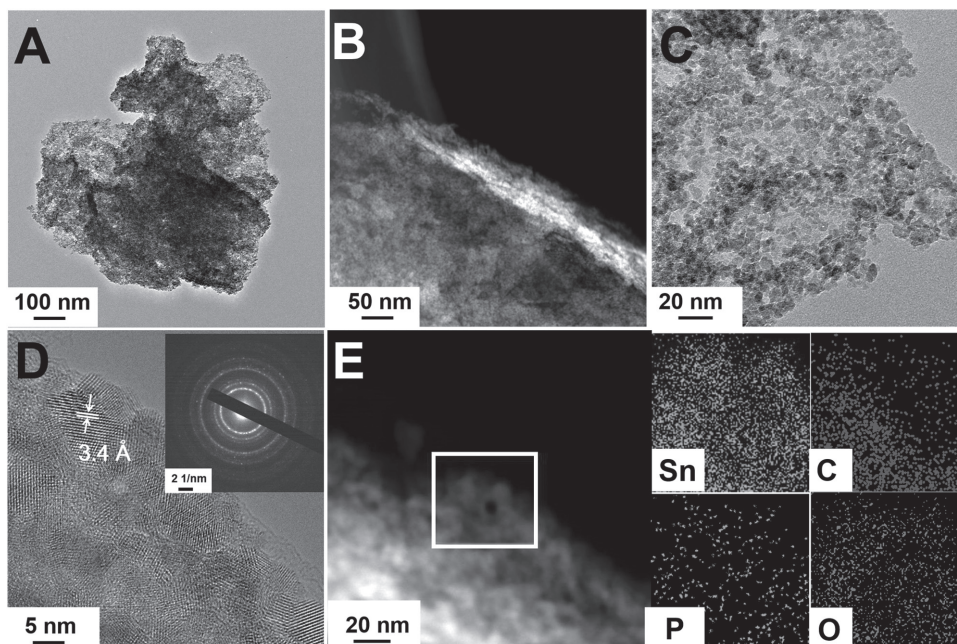

**Figure 1.** The schematic illustrations of formation process of SnO_2/GO and SnO_2@P@GO.

Figure 2. A) TEM image, B) dark field TEM image, and C,D) high-resolution TEM (HRTEM) images of SnO_2@P@GO. E) Elemental mapping showing the distribution of SnO_2@P@GO (up-left: Sn-K mapping, up-right: C-K mapping, bottom-left: P-K mapping, bottom-right: O-K mapping).

only without adding P (Figure S2, Supporting Information) and SnO_2/P/GO is prepared directly by mixing SnO_2/GO and P (Figure S3, Supporting Information).

The X-ray powder diffraction (XRD) pattern in (**Figure 3**A) reveals the phase purity of SnO_2@P@GO, showing three pronounced peaks of 26.5°, 33.8°, and 51.8°, which can be well assigned to (110), (101), and (211) planes of tetragonal SnO_2, respectively. The first broad peak in the XRD pattern may come from phosphorous when compared with the XRD pattern of red phosphorus. Thus, to analyze how P atoms interact with graphene sheets and SnO_2 nanocrystals, Raman spectroscopy, Fourier-transform infrared (FTIR) spectroscopy, and X-ray photoelectron spectroscopy (XPS) are carried out on SnO_2@P@GO. The property of graphene in SnO_2@P@GO, SnO_2/P/GO

composite, and GO is determined by Raman spectra in Figure 3B. The peak at ≈1581 cm^{-1} (G band) corresponds to the E2g mode of graphite, which is related to the vibration of sp^2 bonded carbon atoms in a 2D hexagonal lattice. The peak at ≈1346 cm^{-1} (D band) is an indication of the defects associated with the vacancies, grain boundaries, and amorphous carbon species. The intensity ratio of the D band to the G band (I_D/I_G) is related to the extent of disorder degree and average size of the sp^2 domains. From Figure 3B, the I_D/I_G ratios of SnO_2@P@GO, SnO_2/P/GO composite, and GO are 1.14, 0.97, and 1.07, respectively. The increased I_D/I_G ratio of SnO_2@P@GO indicates the particles on the graphene sheet may form some bonds and break the orderings of graphene. We believe that the electropositive Sn^{4+} in SnO_2 probably has an inductive effect with the phosphorous element, thus resulting
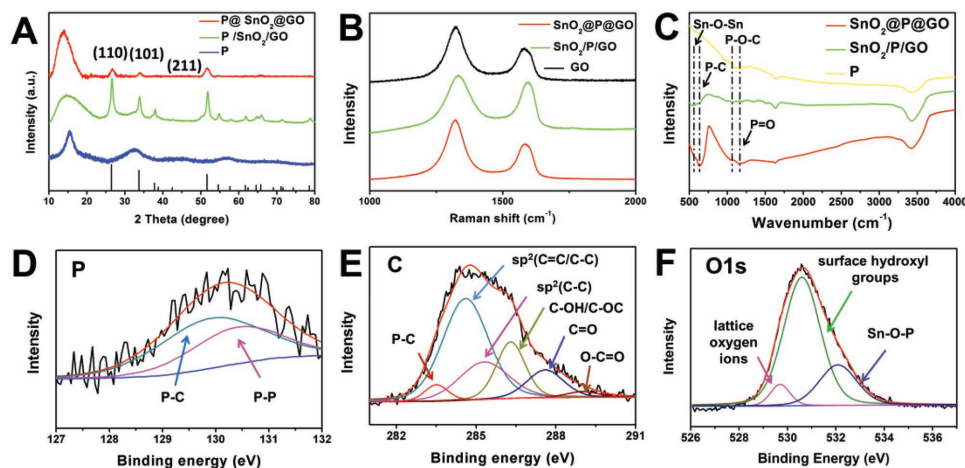
Figure 3. A) XRD patterns of SnO_2@P@GO, SnO_2/P/GO, and red phosphorus. B) Raman spectra of SnO_2@P@GO, SnO_2/P/GO composite, and GO. C) FTIR spectra of SnO_2@P@GO, SnO_2/P/GO, and P. D–F) Chemical composition analysis by XPS for P, C, and O.

in a decrement in crystallinity for the SnO_2@P@GO. FTIR spectra are shown in Figure 3C. A broad peak at 621 cm^{-1} is observed in SnO_2@P@GO, SnO_2/P/GO composite which is assigned to the vibration of Sn−O−Sn, confirming the presence of SnO_2.[42] A sharp increase in peak at 673 cm^{-1} corresponding to P−C bond is observed in SnO_2@P@GO while missing in SnO_2/P/GO, which indicates P−C bond bridges P and graphene.[43,44] However, in SnO_2@P@GO, P−O−C bond located at 1008 cm^{-1} is not observed, indicating that no P−O−C bond is formed.[45] The XPS data in Figure 3D also confirm the existence of P−C bond. The deconvoluted P2p peak in the SnO_2@P@GO shows that there exist both P−P and P−C bonds.[45,46] The content of P−C is 61.19%, indicating that the majority of P is in the form of P−C bond while no P−C bond is found in SnO_2/P/GO (Figure S5, Supporting Information). This is also observed in the deconvoluted C1s peak (Figure 3E). The content of the P–C bond is 3.15% and there exist not only sp^2 bonded carbon but also some sp^3 groups in graphene. Additionally, the O1s spectrum is also deconvoluted (Figure 3E). The main O1s peak at 529.7 eV is associated with lattice oxygen ions.[43] A shoulder at 531.0 eV is attributed to surface hydroxyl groups. The high-energy O 1s peak at 532.0 eV is due to other surface contaminates. The peak at 531.5 eV corresponds to P−O−Sn bonds whose content is 23.56%. No P−O−Sn bonds are observed in SnO_2/P/GO. All these results confirm that the covalent bonds of P−C and P−O−Sn bridge the SnO_2 nanoparticles and graphene by the intermediate P in the SnO_2@P@GO structure.

In order to reveal the content of P, SnO_2, and graphene, thermogravimetric analysis is carried out in air and shown in Figure S6 (Supporting Information). It is found that the weight loss of 17.82% after 700 °C is attributed to the loss of P and graphene. Thus, the content of SnO_2 is 82.18%. To further investigate the composite, inductively coupled plasma (ICP) is carried out and shows that the mass ratio of P and Sn is 1:5.4. Thus, P is 11.97% in the composite and graphene is 5.85% in the composite. The ratio of SnO_2 to graphene is higher than our previous report, indicating the higher loading of SnO_2 on graphene sheet which is consistent with the TEM observations. Additionally, SnO_2@P@GO also shows higher Brunauer–Emmet–Teller (BET) surface area than SnO_2/P/GO due to the much more ordered nanostructure in Figure S4 (Supporting Information) and is able to offer more electrode/electrolyte interface for more active sites during charging/discharging.

In order to evaluate the electrochemical performance, coin cell with lithium metal as anode is assembled. We carefully choose the voltage window of 0.01–1 V in order to avoid the influence of P whose plateau of discharge (lithiation) and charge (delithiation) is located approximately at 1 V.[47,48] In this way, the conversion reaction between Sn and Li_2O which occurs at higher voltages is also prohibited and only the alloying process is taken into account, resulting in the theoretical capacity of 768 mAh g^{-1}. Initially, SnO_2@P@GO is cycled at a low current density of 100 mA g^{-1} and the charge–discharge curves are shown in **Figure 4**A. The initial discharge and charge capacity of SnO_2@P@GO reach 1278 and 405 mAh g^{-1}, respectively, resulting in the coulombic efficiency of 31.7% (Figure S7, Supporting Information). The

large capacity loss during the first cycle is attributed to the formation of SEI layer as well as the irreversible conversion reaction between Sn and Li_2O in the narrow voltage window. The capacities of SnO_2@P@GO and SnO_2/P/GO both increase during the first 30 cycles, which may be associated with the activation process.[41] Despite the large initial loss, SnO_2@P@GO electrodes exhibit very stable cycling performance ever since the second cycle. The capacity of SnO_2@P@GO after 200 cycles is 550 mAh g^{-1}, demonstrating no capacity decay from the 2nd cycle onward. Besides, SnO_2@P@GO manifests the outstanding high-rate cycling stability. Figure 4C shows the cycling performance when the current density is increased to 1000 mA g^{-1}. Remarkably, 95% of the 2nd capacity is retained even after 700 cycles. On the contrast, merely 17% of the 2nd capacity of SnO_2/P/GO is retained after only 300 cycles. In addition, the rate performance is evaluated as well (Figure 4D). The current density is step increased from 0.1 to 1.0 A g^{-1}. The results show that SnO_2@P@GO exhibits excellent rate capability as anode materials for lithium ion batteries. Remarkably, at current density as high as 1.0 A g^{-1}, a capacity of 419 mAh g^{-1} is still achieved, which is 73% of the capacity at 0.1 A g^{-1}. When the current density is recovered to 0.1 A g^{-1}, no capacity decay is observed demonstrating the outstanding rate recovery of SnO_2@P@GO structure. Furthermore, the electrochemical impedance spectrum (EIS) is carried out to provide further insight. Both spectra of SnO_2@P@GO and SnO_2/P/GO show a compressed semicircle from the high to medium frequency range of each spectrum, and a line inclined at ≈45° in the low-frequency range (Figure 4E). The smaller diameter of the semicircle for SnO_2@P@GO electrode in the mid-frequency region (10^1–10^4 Hz) suggests an enhanced conductance of Li$^+$ when compared to the SnO_2/P/GO.

Additionally, we carried out electrochemical kinetics study on this unique structure. The cyclic voltammetry (CV) curves at different scan rates ranging from 0.1 to 1 mV s^{-1} are shown in Figure S8 (Supporting Information). For an electrochemical energy storage device, total capacitive contribution can be quantified and separated by the specific contribution from the capacitive and diffusion-controlled process at a particular voltage according to[49,50]

$$i = k_1v + k_2v^{1/2} \tag{3}$$

where k_1 and k_2 are constants. As shown in Figure S9A (Supporting Information), it is found that the majority of the capacity is covered by shaded region which is the contribution of capacitive behavior at 1 mV s^{-1}. The diffusion-controlled process is mostly around the peak area, indicating that the diffusion process is feasible at regions corresponding to the redox reaction. Furthermore, contribution ratios between the two different processes at other scan rates were calculated in Figure S9B (Supporting Information). The quantified results show that the capacitive contribution gradually improves with increasing the scan rate. Of note, even at a very low scan rate of 0.1 mV s^{-1}, the contribution of capacitive behavior is still very significant (63.2%). It is believed that, the high rate capability is endowed by high capacitive contribution in SnO_2@P@GO.
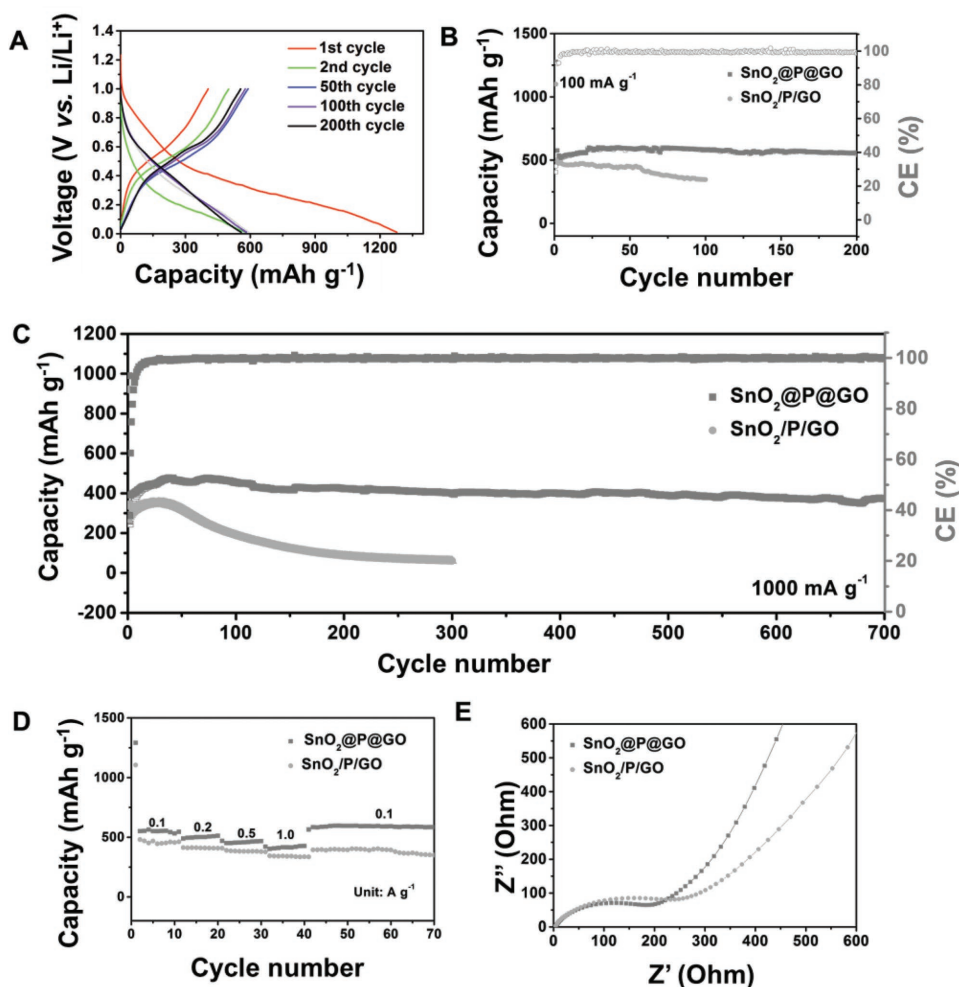
Figure 4. A) Galvanostatic charge–discharge curves of a representative SnO_2@P@GO electrode at 100 mA g^{-1} at different cycles. B) Comparison of cycling stability of SnO_2@P@GO with SnO_2/P/GO at a current density of 100 mA g^{-1}. C) Long-term cycling performance of SnO_2@P@GO composites at a high current density of 1000 mA g^{-1}. D) Rate performance of SnO_2@P@GO and SnO_2/P/GO ranging from 0.1 A g^{-1} to 1 A g^{-1}. E) Nyquist plot of SnO_2@P@GO and SnO_2/P/GO at frequencies from 100 kHz to 0.01 Hz.

We further investigated the stability of chemical bonding through ex situ XPS in Figure S10 (Supporting Information). Initially, in deconvoluted O1s spectrum, we found that a part of lattice oxygen is eliminated while P−O−Sn bonds at 531.5 eV still remain. The content of P−O−Sn is increased to 38.72%, which confirms the stability of P−O−Sn bonds in SnO_2@P@GO after 700 cycles. The deconvoluted P2p peak reveals the existence of P−C bond and the intensity is greatly increased compared to that before cycling. This may be because that P electrochemically reacted with lithium forming Li_3P and P−P bond broke during the first cycle.

To further identify the structure integrity, ex situ TEM images of the SnO_2@P@GO after 700 cycles are shown in **Figure 5**. It can be seen that the nanosheet morphology is preserved very well and the dark field TEM image in Figure 5B shows that there still exist many particles on graphene. Figure 5C shows that the size of SnO_2 nanoparticle increases to around 7 nm and the particle is completely wrapped up the graphene nanosheet with no particles exposed to the electrolyte. This is completely different from our previous report.[40] This further proves the excellent

adhesion between SnO_2 and graphene nanosheets by the bridging phosphorus layer, leading to the excellent integrity. However, the lattice fringes are very ambiguous. Another selected area in Figure 5D shows one SnO_2 nanoparticle in the edge with graphene to see the lattice fringes. Lattice fringes of 2.9 Å corresponding to (200) plane of Sn are observed, indicating that there exists Sn rather than SnO_2 at 1.0 V. However, the fringes are not quite clear which represents the weak crystallization. In addition, the energy dispersive X-ray spectroscopy (EDS) mapping in Figure 5E shows that P, Sn, C, and O all distributed well in the region of the structure, indicating the homogeneous distribution of these elements and confirming the excellent structure integrity. All these results above strongly indicate that despite the increase in particle size, the strong covalent bond between SnO_2 and graphene through P is able to withstand the huge volume variation of SnO_2 and maintain excellent structure integrity as well as electronic connection and buffer the internal stress upon charging/discharging.

Overall, the outstanding electrochemical performance of SnO_2@P@GO can be attributed to the aspects below.
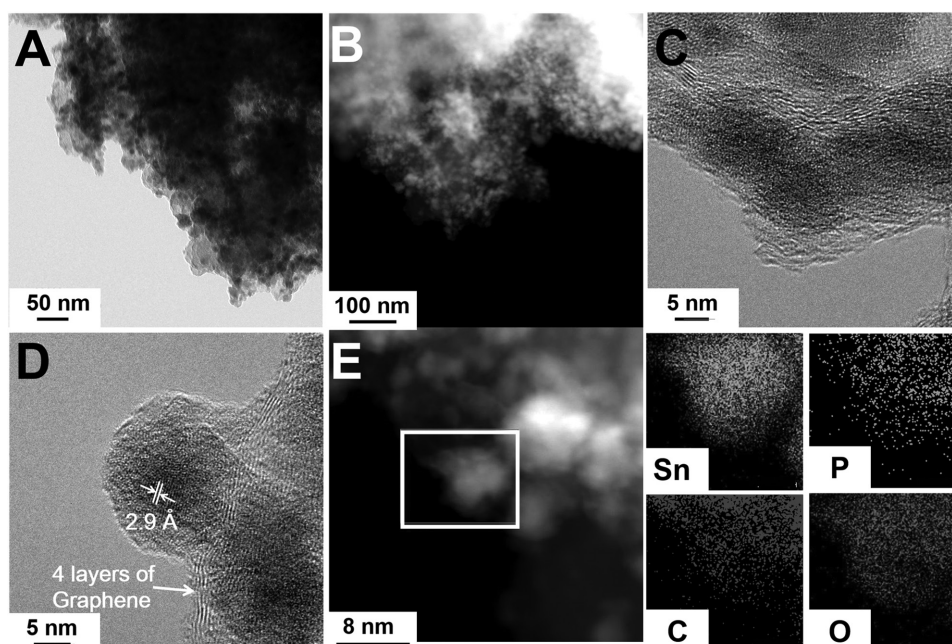
Figure 5. Ex situ characterization of SnO_2@P@GO, A) TEM image, B) dark field TEM image, and C,D) HRTEM images of SnO_2@P@GO after 700 cycles. E) Elemental mapping showing the distribution of SnO_2@P@GO (up-left: Sn-K mapping, up-right: C-K mapping, bottom-left: P-K mapping, bottom-right: O-K mapping).

First, the introduction of P in the nanostructure can helpfully bridge SnO_2 and graphene through covalent bond of P–C and P–O–Sn. During charging/discharging, the covalent bond can well buffer the expansion /contraction of SnO_2 and improve the structure integrity. Second, covalent bonds of P–C and P–O–Sn are stable even after cycling and help to keep the electrical and chemical connection between Sn and graphene. Third, graphene sheet is able to serve as an elastic conductive network and realize fast electron transport. Further, the structure with higher surface area can offer not only large numbers of accessible active sites for lithium-ion insertion. In addition, the small size of tin oxide allows short lithium diffusion length. All their factors are beneficial for the high capacity and rate capability.

3. Conclusions

A facile one-pot approach for preparing SnO_2@P@GO with covalent bonds of P–C and P–O–Sn between SnO_2 and GO is demonstrated. The SnO_2@P@GO exhibits promising performance as the anode for LIB in terms of high capacity (a capacity of 610 mAh g^{-1} at the current density of 100 m A g^{-1}) and outstanding high-rate cycling stability (a capacity retention of 95% at the current density of 1 A g^{-1} after 700 cycles against 2nd cycle). The covalent bonds keep stable after 700 cycles and the structure remains unchanged. These results demonstrate that this kind of unique design is a successful combination of covalent bond of P–C and P–O–Sn resulting in a highly robust structure. It should be noted that even after 700 cycles, the tin oxide particles are totally wrapped up by graphene rather than exposed to the electrolyte which further improves the structure stability.

Such structural design will open up new avenues for the rational design of other sublimatable materials systems, creating new opportunities in the synthesis of advanced functional materials for high-performance energy storage devices.

4. Experimental Section

Preparation of SnO_2@P@GO: The graphene oxide (GO) dispersion was synthesized by the modified Hummer's method. In a typical synthesis, 0.37 g of $SnCl_2$ was mixed with 30 mL ethanolamine and 3 mL of GO dispersion (1.5 mg mL^{-1}) was added after stirring for 10 min. 0.047 g red phosphorus was added into the solution and treated by ultrasonication for 1 h. The suspension was then transferred into an autoclave which had been set to 200 °C for 12 h. After being cooled down to room temperature, the precipitation was then collected and washed with deionized (DI) water and alcohol for several times. After drying for 12 h at 60 °C, the SnO_2@P@GO was obtained.

Material Characterization: XRD measurements were performed on the D8 Discovery diffractometer (Bruker AXS, Karlsruhe, Germany) with a goniometer radius 217.5 mm. XRD patterns were recorded with following measurement conditions: tube voltage of 40 kV, tube current of 40 mA, a coupled two theta mode with three graphs, and each graph taken for 600 s. The microstructures were observed by a field-emission scanning electron microscopy (JEOL-7100F), a TEM and HRTEM (JEM-2100F). BET surface areas were measured by using a Tristar II 3020 instrument. Raman spectra were acquired using a Renishaw RM-1000 laser Raman microscopy system. Thermogravimetry was carried out on a STA449c/3/G (NETZSCH). FTIR transmittance spectra were recorded using a 60-SXB IR spectrometer. XPS measurements were performed using a VG MultiLab 2000 instrument. ICP was carried out on an Optima

4300DV (Perkin Elmer Ltd., USA). As Sn was easily evaporated and led to the loss and inaccuracy, the content of Sn and P was measured separately. For Sn, the sample was dissolved in aqua regia at 90 °C for 2–3 h before measuring. For P, the sample was initially dissolved in 1 mL of concentrated HNO_3, 2 mL of concentrated Hydrofluoric acid (HF) and was heated to 200 °C. After all the liquid was removed, concentrated HCl was added to dissolve the sample.

Electrochemical Characterization: The electrochemical properties were characterized by the assembly of CR2016-type coin cells with lithium metal foil as the anode in a glovebox filled with pure argon gas. The cathode electrodes were composed of 70% active material, 20% acetylene black, and 10% sodium alginate binder. A solution (1 M) of $LiPF_6$ in ethyl carbonate/diethyl carbonate (EC/DMC) (1:1 vol/vol) was used as the electrolyte. Copper foil is used as collector for the coating. The cells were aged for 12 h before charge/discharge process to ensure full filtration of the electrolyte into the electrodes. The capacity was calculated based on the total mass of the composite. The mass loading of each electrode was 1.5–2.0 mg cm^{-2}. Galvanostatic charge/discharge measurement was performed by a multichannel battery testing system (LAND CT2001A), cyclic voltammetry (0.01–1 V) was performed using an electrochemical workstation (CHI 760S), and electrochemical impedance spectroscopy (EIS) was tested with an Autolab Potentiostat Galvanostat (PGSTAT302N). The EIS was carried out at frequency range from 0.1 to 10000 Hz at open circuit potential before cycling to avoid the influence of Li metal. All the measurements were carried out at room temperature. In order to prepare the SEM images after cycling, the electrode was taken out of the disassembled cell and soaked immediately in acetone for 24 h for washing the residue of electrolytes.

Supporting Information

Supporting Information is available from the Wiley Online Library or from the author.

Acknowledgements

[1] K. G. Gallagher, S. Goebel, T. Greszler, M. Mathias, W. Oelerich, D. Eroglu, V. Srinivasan, *Energy Environ. Sci.* **2014**, *7*, 1555.
[2] S. Chu, A. Majumdar, *Nature* **2012**, *488*, 294.
[3] L. Guo, Y. Zhang, J. Wang, L. Ma, S. Ma, Y. Zhang, E. Wang, Y. Bi, D. Wang, W. C. McKee, Y. Xu, J. Chen, Q. Zhang, C. Nan, L. Gu, P. G. Bruce, Z. Peng, *Nat. Commun.* **2015**, *6*, 7898.
[4] J. Liu, L. X. Yuan, K. Yuan, Z. Li, Z. X. Hao, J. W. Xiang, Y. H. Huang, *Nanoscale* **2016**, *8*, 13638.
[5] Q. C. Liu, T. Liu, D. P. Liu, Z. J. Li, X. B. Zhang, Y. Zhang, *Adv. Mater.* **2016**, *28*, 8413.
[6] J. F. Ni, S. D. Fu, C. Wu, J. Maier, Y. Yu, L. Li, *Adv. Mater.* **2016**, *28*, 2259.
[7] F. Zou, X. Hu, Z. Li, L. Qie, C. Hu, R. Zeng, Y. Jiang, Y. Huang, *Adv. Mater.* **2014**, *26*, 6622.
[8] L. Wang, D. Wang, Z. Dong, F. Zhang, J. Jin, *Nano Lett.* **2013**, *13*, 1711.
[9] H. W. Song, G. Z. Yang, H. Cui, C. X. Wang, *Nano Energy* **2014**, *3*, 16.
[10] B. Luo, L. J. Zhi, *Energy Environ. Sci.* **2015**, *8*, 456.
[11] Y. L. Ding, Y. Wen, C. Wu, P. A. V. Aken, J. Maier, Y. Yu, *Nano Lett.* **2015**, *15*, 1388.
[12] D. Bresser, S. Passerini, B. Scrosati, *Energy Environ. Sci.* **2016**, *9*, 3348.
[13] Z. Li, J. Ding, D. Mitlin, *Acc. Chem. Res.* **2015**, *48*, 1657.
[14] B. Luo, T. F. Qiu, D. L. Ye, L. Z. Wang, L. J. Zhi, *Nano Energy* **2016**, *22*, 232.
[15] H. M. Oh, H. Jeong, G. H. Han, H. Kim, J. H. Kim, S. Y. Lee, S. Y. Jeong, S. Jeong, D. J. Park, K. K. Kim, Y. H. Lee, M. S. Jeong, *ACS Nano* **2016**, *10*, 10446.
[16] J. Patra, H. C. Chen, C. H. Yang, C. T. Hsieh, C. Y. Su, J. K. Chang, *Nano Energy* **2016**, *28*, 124.
[17] Y. J. Hong, Y. C. Kang, *Carbon* **2015**, *88*, 262.
[18] J. Zhu, G. H. Zhang, X. Z. Yu, Q. H. Li, B. G. Lu, Z. Xu, *Nano Energy* **2014**, *3*, 80.
[19] S. Y. Lee, K. Y. Park, W. S. Kim, S. Yoon, S. H. Hong, K. Kang, M. Kim, *Nano Energy* **2016**, *19*, 234.
[20] J. H. Sun, L. H. Xiao, S. D. Jiang, G. X. Li, Y. Huang, J. X. Geng, *Chem. Mater.* **2015**, *27*, 4594.
[21] B. Huang, X. H. Li, Y. Pei, S. Li, X. Cao, R. C. Massé, G. Z. Cao, *Small* **2016**, *12*, 1945.
[22] J. Liang, X. Y. Yu, H. Zhou, H. B. Wu, S. J. Ding, X. W. Lou, *Angew. Chem. Int. Ed.* **2014**, *53*, 12803.
[23] W. Li, S. L. Chou, J. Z. Wang, J. H. Kim, H. K. Liu, S. X. Dou, *Adv. Mater.* **2014**, *26*, 4037.
[24] G. D. Park, J. K. Lee, Y. C. Kang, *Adv. Funct. Mater.* **2017**, *27*, 1603399.
[25] V. Etacheri, G. A. Seisenbaeva, J. Caruthers, G. Daniel, J. M. Nedelec, V. G. Kessler, V. G. Pol, *Adv. Energy Mater.* **2015**, *5*, 1401289.
[26] S. Yang, W. B. Yue, J. Zhu, Y. Ren, X. J. Yang, *Adv. Funct. Mater.* **2013**, *23*, 3570.
[27] X. Zhou, L. J. Wan, Y. G. Guo, *Adv. Mater.* **2013**, *25*, 2152.
[28] W. W. Xu, K. N. Zhao, C. J. Niu, L. Zhang, Z. Y. Cai, C. H. Han, L. He, T. Shen, M. Y. Yan, L. B. Qu, L. Q. Mai, *Nano Energy* **2014**, *8*, 196.
[29] Z. Q. Zhu, S. W. Wang, J. Du, Q. Jin, T. R. Zhang, F. Y. Cheng, J. Chen, *Nano Lett.* **2014**, *14*, 153.
[30] K. N. Zhao, M. Y. Wen, Y. F. Dong, L. Zhang, M. Y. Yan, W. W. Xu, C. J. Niu, L. Zhou, Q. L. Wei, W. H. Ren, X. D. Wang, L. Q. Mai, *Adv. Energy Mater.* **2016**, DOI: 10.1002/aenm.201601582.
[31] X. Wang, G. Li, M. H. Seo, F. M. Hassan, M. A. Hoque, Z. Chen, *Adv. Energy Mater.* **2015**, *5*, 1501106.
[32] H. L. Wang, Y. Yang, Y. Y. Liang, G. Y. Zheng, Y. Y. Li, Y. Cui, H. J. Dai, *Energy Environ. Sci.* **2012**, *5*, 7931.
[33] Y. S. Ye, X. L. Xie, J. Rick, F. C. Chang, B. J. Hwang, *J. Power Sources* **2014**, *247*, 991.
[34] Y. Y. Liang, Y. G. Li, H. L. Wang, H. J. Dai, *J. Am. Chem. Soc.* **2013**, *135*, 2013.
[35] Y. Y. Liang, H. L. Wang, J. G. Zhou, Y. G. Li, J. Wang, T. Regier, H. J. Dai, *J. Am. Chem. Soc.* **2012**, *134*, 3517.

[36] X. L. Wang, G. Li, F. M. Hassan, J. D. Li, X. Y. Fan, R. Batmaz, X. C. Xiao, Z. W. Chen, *Nano Energy* **2015**, *15*, 746.

[37] F. M. Hassan, R. Batmaz, J. Li, X. Wang, X. Xiao, A. Yu, Z. Chen, *Nat. Commun.* **2015**, *6*, 8597.

[38] Y. Y. Liang, Y. G. Li, H. L. Wang, J. G. Zhou, J. Wang, T. Regier, H. J. Dai, *Nat. Mater.* **2011**, *10*, 780.

[39] E. G. da Silveira Firmiano, A. C. Rabelo, C. J. Dalmaschio, A. N. Pinheiro, E. C. Pereira, W. H. Schreiner, E. R. Leite, *Adv. Energy Mater.* **2014**, *4*, 1301380.

[40] Y. Yao, N. Liu, M. T. McDowell, M. Pasta, Y. Cui, *Energy Environ. Sci.* **2012**, *5*, 7927.

[41] K. N. Zhao, L. Zhang, R. Xia, Y. F. Dong, W. W. Xu, C. J. Niu, L. He, M. Y. Yan, L. B. Qu, L. Q. Mai, *Small* **2016**, *12*, 588.

[42] L. Zhang, K. N. Zhao, W. W. Xu, Y. F. Dong, R. Xia, F. N. Liu, L. He, Q. L. Wei, M. Y. Yan, L. Q. Mai, *Phys. Chem. Chem. Phys.* **2015**, *17*, 7619.

[43] J. Cha, T. Kubo, H. Takebe, M. Kuwabara, *J. Ceram. Soc. Jpn.* **2008**, *116*, 915.

[44] L. W. Daasch, D. C. Smith, *Anal. Chem.* **1951**, *23*, 853.

[45] J. X. Song, Z. X. Yu, M. L. Gordin, S. Hu, R. Yi, D. H. Tang, T. Walter, M. Regula, D. Choi, X. Li, A. Manivannan, D. Wang, *Nano Lett.* **2014**, *14*, 6329.

[46] J. Sun, G. Zheng, H. W. Lee, N. Liu, H. Wang, H. Yao, W. Yang, Y. Cui, *Nano Lett.* **2014**, *14*, 4573.

[47] J. F. Qian, D. Qiao, X. P. Ai, Y. L. Cao, H. X. Yang, *Chem. Commun.* **2012**, *48*, 8931.

[48] C. Zhu, P. Yang, D. Chao, X. Wang, X. Zhang, S. Chen, B. K. Tay, H. Huang, H. Zhang, W. Mai, H. J. Fan, *Adv. Mater.* **2015**, *27*, 4566.

[49] L. Zhang, K. N. Zhao, Y. Z. Luo, Y. F. Dong, W. W. Xu, M. Y. Yan, W. H. Ren, L. Zhou, L. B. Qu, L. Q. Mai, *ACS Appl. Mater. Interfaces* **2016**, *8*, 7139.

[50] K. N. Zhao, F. N. Liu, C. J. Niu, W. W. Xu, Y. F. Dong, L. Zhang, S. M. Xie, M. Y. Yan, Q. L. Wei, D. Y. Zhao, L. Q. Mai, *Adv. Sci.* **2015**, *2*, 1500154.